



Highly efficient photocatalytic H₂ evolution from water over CdLa₂S₄/mesoporous g-C₃N₄ hybrids under visible light irradiation

Hong Liu*, Zhengzheng Xu, Zhe Zhang, Dan Ao

Department of Chemical Engineering, School of Environmental and Chemical Engineering, Shanghai University, 99 Shangda Road, Shanghai 200444, PR China

ARTICLE INFO

Article history:

Received 2 December 2015

Received in revised form 20 March 2016

Accepted 31 March 2016

Available online 31 March 2016

Keywords:

g-C₃N₄

CdLa₂S₄

Mesoporous

Hydrogen evolution

Visible light

ABSTRACT

In this study, mesoporous graphitic carbon nitride (mpg-C₃N₄) nanosheets with high surface area (317 m² g⁻¹) were obtained by using SBA-15 as a hard-template, and CdLa₂S₄ nanoparticles were successfully grown on these mpg-C₃N₄ nanosheets via a facile hydrothermal method. The as-synthesized CdLa₂S₄/mpg-C₃N₄ hybrids were characterized by X-ray diffraction (XRD), transmission electron microscopy (TEM), high-resolution transmission electron microscopy (HRTEM), energy-dispersive X-ray spectroscopy (EDS), X-ray photoelectron spectroscopy (XPS), N₂ adsorption-desorption, ultraviolet–visible diffuse reflection spectroscopy (DRS). Compared with pure CdLa₂S₄, the CdLa₂S₄/mpg-C₃N₄ hybrid materials displayed higher photocatalytic H₂ evolution performance under the visible light (λ > 420 nm) using Na₂S and Na₂SO₃ as the sacrificial agent. The optimal content of mpg-C₃N₄ was about 20 wt% and the corresponding photocatalytic H₂ evolution was 5984.8 μmol h⁻¹ g⁻¹ (with an apparent quantum efficiency of 7.1% at 420 nm), which was 7.7 times higher than that of pure CdLa₂S₄. The results of photoluminescence (PL) and photocurrent response demonstrated that the recombination of photo-generated electron-hole pairs was effectively inhibited due to the well-matched band structure and intimate contact interfaces of CdLa₂S₄ and mpg-C₃N₄. Based on the results and analysis, a possible enhanced photocatalytic activity mechanism of CdLa₂S₄/mpg-C₃N₄ composites was also proposed.

© 2016 Elsevier B.V. All rights reserved.

1. Introduction

The increasing global energy crisis has led to the search for new clean and renewable energy resources. Since TiO₂ electrode of photoelectrochemical water splitting has been discovered by Honda [1] in 1972, photocatalytic hydrogen production via semiconductor photocatalysts has been considered as the most promising method of producing clean energy from renewable solar energy [2–5]. So far, a variety of active photocatalysts for hydrogen production, including metal oxides [6,7], sulfides [5,8], oxynitrides [9], as well as the metal-free semiconductors [10] have already been developed.

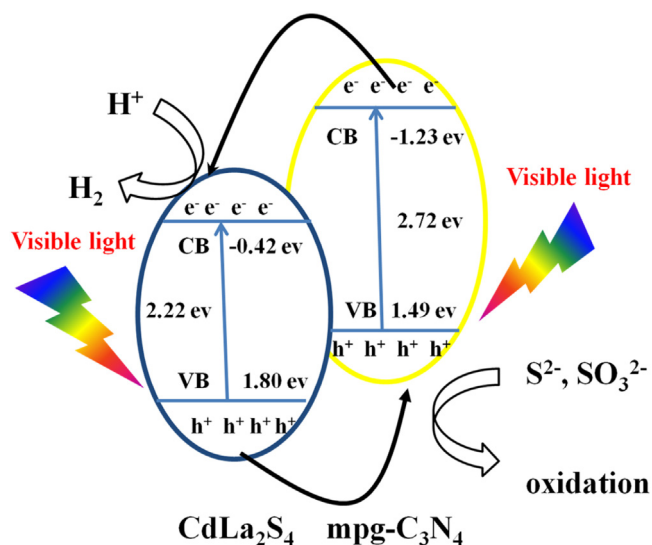
Among the numerous types of semiconductor systems studied, metal sulfides have demonstrated promising activities toward hydrogen evolution from water containing sacrificial reagents under visible light [5,8,11,12]. CdLa₂S₄ is a ternary chalcogenide with a suitable band gap (2.1–2.4 eV) [11,13], well corresponding to the visible light absorption. Previous studies revealed that CdLa₂S₄ is active for photocatalytic hydrogen generation and degradation

of organic pollutants under visible light irradiations [11,13]. For example, Kale et al. [11] synthesized CdLa₂S₄ hexagon flowers, nanoprisms and nanowires via a facile hydrothermal method and found that the obtained CdLa₂S₄ exhibited efficient photocatalytic activity for hydrogen production under solar light. Xing et al. [13] reported the synthesis of CdLa₂S₄ microspheres and its application in photocatalytic removal of methyl orange. However, the photocatalytic activity over pure CdLa₂S₄ is low because of the poor separation efficiency and low migration ability of the photoexcited charge carriers. To enhance the photocatalytic performance of CdLa₂S₄, some efforts have been made. For instance, by deposition of Ag or incorporation of metal sulfides into CdLa₂S₄, the photocatalytic performance of CdLa₂S₄ has been enhanced to a certain degree [14–16]. Nevertheless, Pt-loading was still required for H₂ evolution [15,16]. So the photocatalytic activity of CdLa₂S₄ still needs to be further improved.

Recently, graphitic carbon nitride (g-C₃N₄) with visible-light-driven bandgap (~2.7 eV) and proper band positions, has been widely applied in photocatalytic hydrogen evolution, degradation of pollutants, CO₂ reduction and photocatalytic organic synthesis [10,17–20]. However, bulk g-C₃N₄ exhibits low photocatalytic activity under visible light owing to its low surface area (less than

* Corresponding author.

E-mail address: liuhong@shu.edu.cn (H. Liu).



Scheme 1. Proposed photocatalytic H_2 production and charge transfer mechanisms of $\text{CdLa}_2\text{S}_4/\text{mpg-C}_3\text{N}_4$ composites.

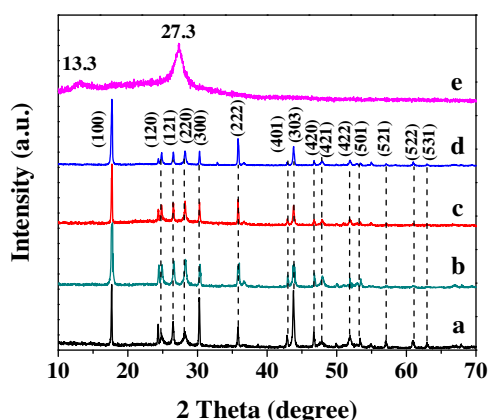


Fig 1. The XRD patterns of as-prepared samples: (a) CdLa_2S_4 , (b) CLSCN10, (c) CLSCN20, (d) CLSCN30, (e) $\text{mpg-C}_3\text{N}_4$.

$10 \text{ m}^2 \text{ g}^{-1}$) and poor quantum yield (0.1% at 420–460 nm) [10,17], so a number of strategies have been employed to modify bulk $\text{g-C}_3\text{N}_4$. To increase the specific surface area and provide more active sites for adsorption and photocatalytic reaction, various soft or hard templates are usually employed to introduce pores in $\text{g-C}_3\text{N}_4$ [21–23]. Previous researches have indicated that porous $\text{g-C}_3\text{N}_4$ exhibit much higher photocatalytic ability than its bulk counterparts due to its large surface area and multiple scattering effects [23,24]. To increase the quantum yield of $\text{g-C}_3\text{N}_4$, many methods have been developed to inhibit the recombination of photogenerated electron-hole pairs, such as doping with metal or nonmetal elements [25–28], and coupling with noble metal [29,30], graphene [31], or other semiconductors [32–34]. Among them, coupling $\text{g-C}_3\text{N}_4$ with other components is a promising strategy for improving the charge separation in photocatalysis, especially when the nano-junction structure is formed in the composites.

When examining the band-edge position of CdLa_2S_4 and $\text{g-C}_3\text{N}_4$, it is found that both the conduction band (CB) and valence band (VB) of $\text{g-C}_3\text{N}_4$ are more negative than that of CdLa_2S_4 . Under visible light illumination, the photogenerated electrons will transfer from the CB of $\text{g-C}_3\text{N}_4$ to that of CdLa_2S_4 , while the holes on VB of CdLa_2S_4 will migrate to that of $\text{g-C}_3\text{N}_4$, achieving the separation of charge carriers in composites. Therefore, it can be expected that combining CdLa_2S_4 with $\text{g-C}_3\text{N}_4$ may result in an improved photocatalytic

efficiency compared with individual $\text{g-C}_3\text{N}_4$ and CdLa_2S_4 . However, to the best of our knowledge, the coupling of CdLa_2S_4 with $\text{g-C}_3\text{N}_4$ for photocatalytic purposes has not been reported previously.

In this research, mesoporous $\text{g-C}_3\text{N}_4$ ($\text{mpg-C}_3\text{N}_4$) nanosheets supported CdLa_2S_4 nanocomposites were synthesized through a hard-template combined with hydrothermal method. The obtained $\text{CdLa}_2\text{S}_4/\text{mpg-C}_3\text{N}_4$ composites exhibited significantly enhanced visible-light photocatalytic H_2 evolution performance compared with pristine CdLa_2S_4 and $\text{mpg-C}_3\text{N}_4$. No noticeable decreases in the activity of as-prepared $\text{CdLa}_2\text{S}_4/\text{mpg-C}_3\text{N}_4$ photocatalysts were observed during the photocatalytic H_2 -production. A possible enhancement mechanism for the improved photocatalytic activity in the $\text{CdLa}_2\text{S}_4/\text{mpg-C}_3\text{N}_4$ composites was also proposed.

2. Experimental

2.1. Materials

Mesoporous silica SBA-15 ($S_{\text{BET}} = 514 \text{ m}^2 \text{ g}^{-1}$) was purchased from Tanlian Co., Ltd. (Shanghai, China). Other chemicals used in the experiments were purchased from Sinopharm Chemical Reagent Co., Ltd. (Shanghai, China). All chemicals used in the experiments are of analytical grade and were used without further purification.

2.2. Synthesis

2.2.1. Preparation of $\text{mpg-C}_3\text{N}_4$ nanosheets

Mesoporous $\text{g-C}_3\text{N}_4$ nanosheets were prepared by a hard-template method using cyanamide and SBA-15 as a precursor and hard-template, respectively. In detail, 1.2 g SBA-15 was impregnated into 16.0 g cyanamide (50 wt%) aqueous solution, and kept stirring at 70°C for 4 h. Then, the resultant mixture was centrifuged, dried and finally calcined at 550°C for 4 h. The obtained powder was treated with 10 wt% HF for 48 h to remove the silica template. The light yellow $\text{mpg-C}_3\text{N}_4$ nanosheets were collected by centrifugation, washed with water and ethanol several times, and dried at 80°C .

2.2.2. Preparation of $\text{CdLa}_2\text{S}_4/\text{mpg-C}_3\text{N}_4$ composites

The $\text{CdLa}_2\text{S}_4/\text{mpg-C}_3\text{N}_4$ composites were prepared by a hydrothermal method. Firstly, $0.74 \text{ g Cd}(\text{NO}_3)_2 \cdot 4\text{H}_2\text{O}$, $1.67 \text{ g La}(\text{NO}_3)_3 \cdot 6\text{H}_2\text{O}$ and 1.42 g thiourea was dispersed in a mixed solution containing 5 mL ethanol and 15 mL deionized water. Secondly, an appropriate amount of as-prepared $\text{mpg-C}_3\text{N}_4$ nanosheets were dispersed in 20 mL distilled water by ultrasound for 30 min. Then, the obtained $\text{mpg-C}_3\text{N}_4$ solution was added dropwise to above solution under magnetic stirring for 2 h until milk-like mixture formed. The homogeneous solution was then transferred into a 100 mL Teflon-lined stainless steel autoclave and maintained at 160°C for 72 h. Lastly, the yellow products were collected by centrifugation and washed several times with distilled water and ethanol, and dried at 80°C for 12 h. The as-synthesized $\text{CdLa}_2\text{S}_4/\text{mpg-C}_3\text{N}_4$ sample with 10 wt%, 20 wt% and 30 wt% $\text{mpg-C}_3\text{N}_4$ was labeled as CLSCN10, CLSCN20 and CLSCN30, respectively. For comparison, pure CdLa_2S_4 was prepared using the same hydrothermal method without the addition of $\text{mpg-C}_3\text{N}_4$.

2.3. Characterization

The crystal structure of the samples was investigated using X-ray diffraction (XRD, D/MAX-2550, $\lambda = 0.15418 \text{ nm}$) with $\text{Cu K}\alpha$ radiation. The morphologies of the samples were measured by transmission electron microscopy (TEM, JEOL 200CX) and high-resolution transmission electron microscopy (HRTEM, JEM-2010F). X-ray photoelectron spectroscopy (XPS) measurements were performed on a PHI ESCA-5000C electron spectrometer. FT-IR spectra

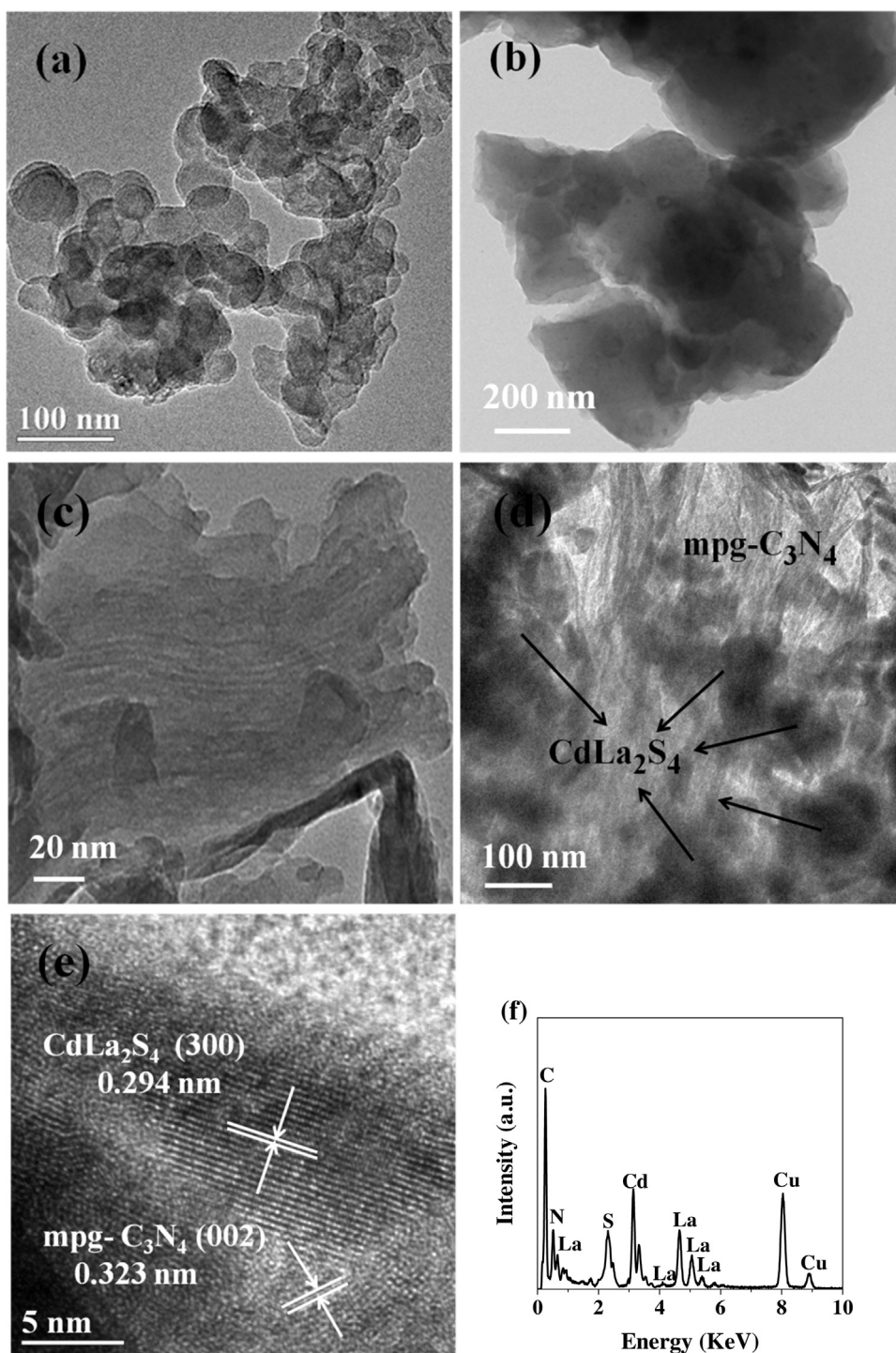


Fig. 2. TEM images of (a) CdLa_2S_4 , (b) and (c) $\text{mpg-C}_3\text{N}_4$, (d) CLSCN20, (e) HRTEM image and (f) EDS spectrum of CLSCN20.

were recorded at room temperature using a FT-IR spectrophotometer (AVATAR3700). N_2 adsorption-desorption isotherms were obtained at -196°C on a Micromeritics ASAP 2010 Sorptometer using static adsorption procedures, and the BET surface areas and pore size distributions were calculated by using N_2 adsorption-desorption isotherms. UV-vis absorption spectra over a range of 200–800 nm were analyzed by a UV-vis spectrophotometer (Hitachi U-3010) equipped with an integration sphere and using BaSO_4 as the reference. The photoluminescence (PL) spectra of the photocatalyst were obtained using a Hitachi F-7000 fluorescence spectrophotometer at room temperature.

2.4. Photocurrent measurements

The photocurrent measurements were carried out on a CHI660E electrochemical instrument in a standard three-electrode system with Pt foil as counter electrode and Ag/AgCl as the reference electrode. The working electrode was prepared as follows: 10 mg of the as-prepared photocatalyst was suspended in 1 mL ethanol to produce a slurry, which was then dip-coated onto an indium tin oxide (ITO) glass electrode. The coated area on the ITO glass was controlled to be 0.283 cm^2 . The film was dried in air and subsequently calcined at 120°C for 6 h. A 300 W Xe arc lamp with a UV-cut off

filter ($\lambda > 420$ nm) was used as the photosource and Na_2SO_4 (0.5 M) aqueous solution was used as the electrolyte.

2.5. Photocatalytic activity measurement

The photocatalytic hydrogen evolution experiments were performed in a 100 mL quartz reactor at room temperature connected to a closed-cycle circulation system. The visible light was provided by a 300 W Xenon lamp (PLS-SXE300C, Beijing Perfectlight Co. Ltd., China) coupled with a UV cut-off filter ($\lambda > 420$ nm). In a typical experiment, 0.05 g of photocatalyst powder was dispersed in 100 mL of aqueous solution containing 0.1 M Na_2S and 0.5 M Na_2SO_3 . The reaction vessel was evacuated by N_2 for 30 min to remove dissolved oxygen before photocatalytic experiments. The reaction cell was kept at room temperature with cooling water. The produced H_2 was detected using an online gas chromatography (GC7900, N_2 carrier, 5A molecular sieve column, TCD detector).

The apparent quantum efficiency (QE) for H_2 evolution was also measured under the same photocatalytic reaction conditions, only with a band-pass filter of 420 nm. The average intensity of irradiation was measured as 15.0 mW cm^{-2} (PL-MW2000 spectroradiometer) and the irradiation area was controlled at 28.26 cm^2 . The QE was calculated according to following equation:

$$\text{QE} = \frac{2 \times R_{\text{H}_2}}{I} \times 100\%$$

where R_{H_2} and I represent the H_2 evolution rate at 420 nm (molecules h^{-1}), and the rate of absorption of incident photons, respectively.

3. Results and discussion

3.1. Structure and properties characterization

Fig. 1 shows the XRD patterns of mpg- C_3N_4 nanosheets, CdLa_2S_4 and $\text{CdLa}_2\text{S}_4/\text{mpg-}\text{C}_3\text{N}_4$ composites with different g- C_3N_4 contents. The mpg- C_3N_4 sample exhibits an intense diffraction peak located at 27.3° and a weak one observed at 13.3° , which corresponds to the (002) and (100) diffraction plane of g- C_3N_4 , respectively (JCPDS 87-1526). For pure CdLa_2S_4 sample, all the diffraction peaks can be indexed to CdLa_2S_4 and no other phases, such as CdS and La_2S_3 , are observed, which demonstrates the single CdLa_2S_4 phase with high crystallinity is obtained [11,15]. No significant peaks of g- C_3N_4 can be detected in the $\text{CdLa}_2\text{S}_4/\text{mpg-}\text{C}_3\text{N}_4$ samples due to the low X-ray diffraction intensity of the mpg- C_3N_4 nanosheets. Nevertheless, the presence of g- C_3N_4 nanosheets in the composites can be confirmed by TEM, FTIR and XPS analyses.

The morphology and microstructure of the as-prepared samples were examined by the transmission electron microscopy (TEM) and high-resolution transmission electron microscopy (HRTEM). As shown in Fig. 2a, CdLa_2S_4 was mainly present as sphere-like morphology with a size around 50 nm. The pure mpg- C_3N_4 displays a two-dimensional layered structure (Fig. 2b), and a high-magnification TEM image recorded along the (110) direction shown in Fig. 2c reveals that they have ordered mesostructures, which is similar to the mesochannels of SBA-15 [21]. The corresponding pore diameter of nanochannels, as indicated by the bright lines passing through the mpg- C_3N_4 matrix, is calculated as about 3.6 nm. Fig. 2d indicates that the CdLa_2S_4 nanoparticles are attached to the nanosheets surface of mpg- C_3N_4 to form the heterojunction structures with intimate interfacial contact. This intimate contact will facilitate the transfer of photogenerated charge and improve the photocatalytic performance. The HRTEM image of CLSCN20 shown in Fig. 2e reveals two different kinds of lattice fringes about 0.294 and 0.323 nm, which are characteristic of (300) lattice plane of CdLa_2S_4 and the (002) crystal plane of mpg- C_3N_4 , respectively

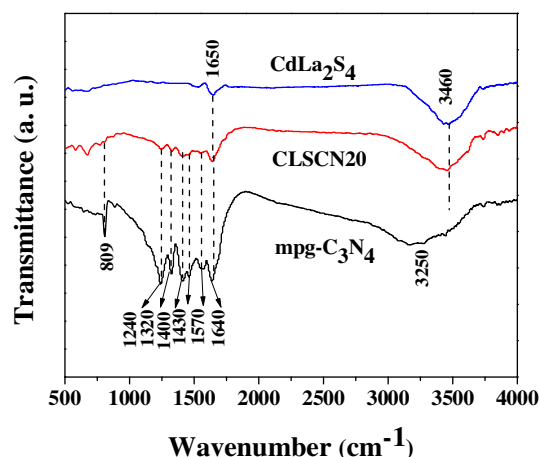


Fig. 3. FT-IR spectra of pure mpg- C_3N_4 , CdLa_2S_4 and CLSCN20.

[14,15,35]. The EDS spectrum of CLSCN20 (Fig. 3f) demonstrates that the $\text{CdLa}_2\text{S}_4/\text{mpg-}\text{C}_3\text{N}_4$ composite contains Cd, La, S, C and N elements.

Fig. 3 shows the FT-IR spectra of mpg- C_3N_4 , CdLa_2S_4 and the $\text{CdLa}_2\text{S}_4/\text{mpg-}\text{C}_3\text{N}_4$ (20%) sample. In the FT-IR spectra of mpg- C_3N_4 , the broad peak at 3250 cm^{-1} can be attributed to stretching mode of the N–H bond [36]. And the peaks located at about 1240, 1320, 1400, 1430, 1570 and 1640 cm^{-1} are ascribed to aromatic C–N stretching vibration modes and C=N stretching vibration modes [31,37]. The peak at 809 cm^{-1} is originated from characteristic breathing vibration of triazine ring [37]. For the pure CdLa_2S_4 , the peak at 1650 and 3460 cm^{-1} are related to OH^- on the surface of CdLa_2S_4 [38]. In the case of the $\text{CdLa}_2\text{S}_4/\text{mpg-}\text{C}_3\text{N}_4$ composite, the IR bands characteristic of mpg- C_3N_4 and CdLa_2S_4 are also identified, confirming that the composite photocatalyst is composed of mpg- C_3N_4 and CdLa_2S_4 .

The surface chemical composition of mpg- C_3N_4 , CdLa_2S_4 and CLSCN20 and the interaction of mpg- C_3N_4 with CdLa_2S_4 were analyzed by X-ray photoelectron spectroscopy (XPS). The XPS survey spectrum of CLSCN20 (Fig. 4a) confirms that the composite is mainly composed of C, N, Cd, La and S. The C 1s spectrum of mpg- C_3N_4 shown in Fig. 4b can be deconvoluted into three peaks located at 284.8, 286.4 and 288.2 eV , which is assigned to C–C coordination containing adventitious hydrocarbon from the XPS instrument and sp^2 -hybridized carbon atoms present, C=N or C≡N coordination and C–N bonds, respectively [31,37]. The N 1s spectrum of mpg- C_3N_4 (Fig. 4c) can be divided into three peaks centered at 398.4, 399.7 and 400.9 eV , corresponding to the nitrogen atoms in the aromatic rings (C=N–C), tertiary nitrogen (N–(C)₃) and C–N–H, respectively [39,40]. Compared with mpg- C_3N_4 , the C 1s and N 1s peaks of CLSCN20 exhibit a positive shift, indicating the mpg- C_3N_4 structure has changed after interaction with CdLa_2S_4 to form the heterojunction. As shown in Fig. 4d, the Cd 3d peaks of pure CdLa_2S_4 at 405.2 eV (Cd $3d_{5/2}$) and 411.9 eV (Cd $3d_{3/2}$) are ascribed to Cd^{2+} in CdLa_2S_4 [11,15], while the binding energy of Cd $3d_{5/2}$ and Cd $3d_{3/2}$ of CLSCN20 are 404.9 and 411.6 eV . The La 3d peaks of pure CdLa_2S_4 (Fig. 4e) locate at 835.3 eV (La $3d_{5/2}$), 838.2 eV (La $3d_{5/2}$), 852.2 eV (La $3d_{3/2}$) and 855.1 eV (La $3d_{3/2}$), which are in good agreement with the previous work [11,15,41–43]. The main peaks located at 835.3 and 852.2 eV are ascribed to La^{3+} in the sample [41–43]. The satellite peaks of La $3d_{5/2}$ and La $3d_{3/2}$ at 838.2 and 855.1 eV might be attributed to the defects that are present in the crystals [43]. The binding energies of La $3d_{5/2}$ and La $3d_{3/2}$ of CLSCN20 are 835.5 eV , 839.2 eV , 852.6 eV and 855.6 eV , which are higher than that of pure CdLa_2S_4 . A similar phenomenon is also found in the XPS spectra of S 2p (Fig. 4f). The binding energies of S $2p_{3/2}$ (161.4 eV) and S $2p_{1/2}$

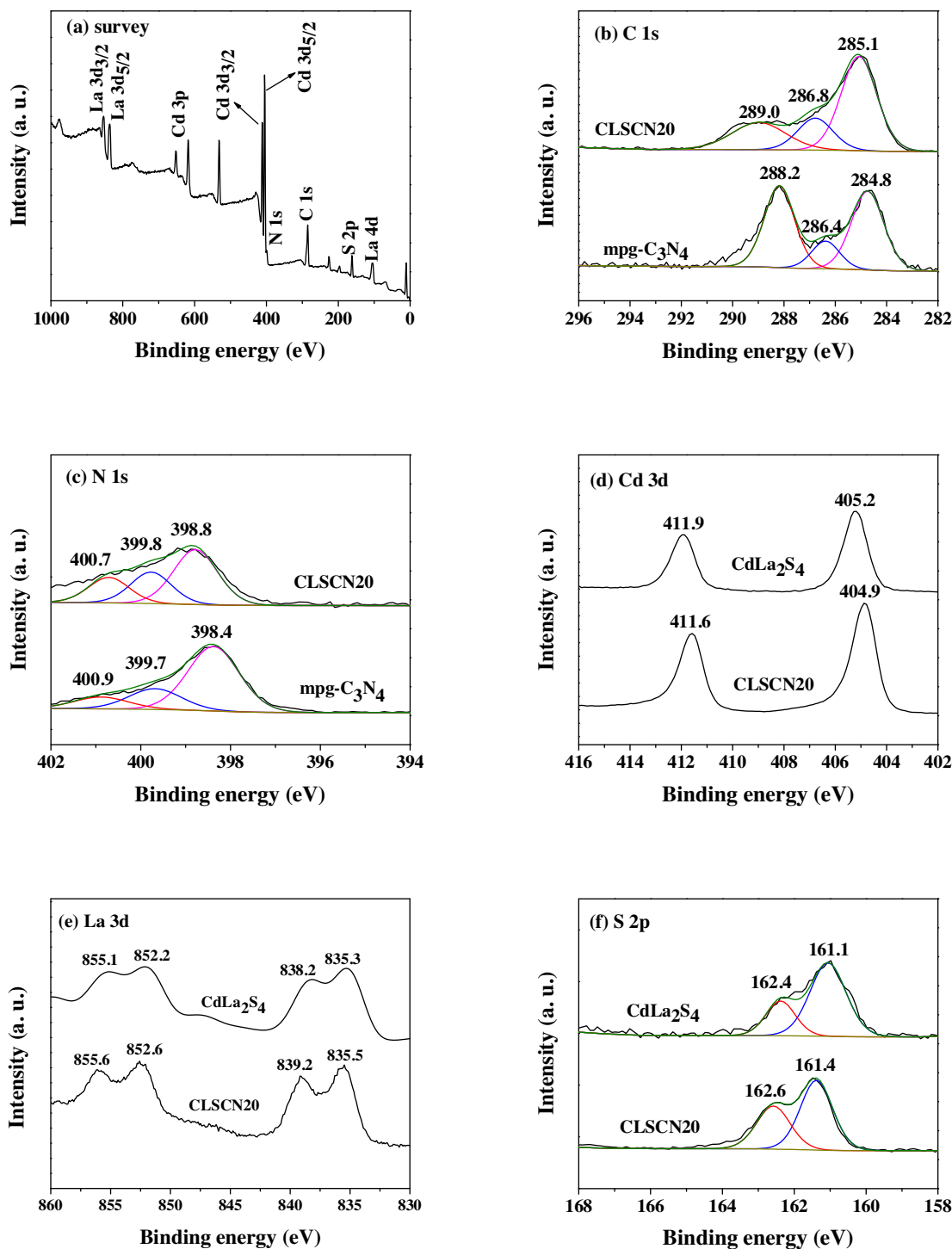


Fig. 4. XPS spectra of mpg-C₃N₄, CdLa₂S₄ and CLSCN20: (a) survey of CLSCN20, (b) C 1s, (c) N 1s, (d) Cd 3d, (e) La 3d, (f) S 2p.

(162.6 eV) of CLSCN20 are higher than that of pure CdLa₂S₄. The results demonstrate that the presence of chemical bonds between mpg-C₃N₄ and CdLa₂S₄, rather than a simple physical mixture.

The optical properties of the CdLa₂S₄/mpg-C₃N₄ composites with different amounts of mpg-C₃N₄ were analyzed by the UV–vis absorption spectroscopy and the results are shown in Fig. 5. Pure mpg-C₃N₄ sample shows absorption wavelengths from the UV to the visible range up to 460 nm. For CdLa₂S₄, the absorption edge is about 580 nm, exhibiting the broad absorption region of visible-light. The CdLa₂S₄/mpg-C₃N₄ composites have absorption edges to longer wavelengths in comparison with the pure mpg-C₃N₄. The

observations are attributed to the interaction between mpg-C₃N₄ and CdLa₂S₄ in the composites [12,40]. The interaction probably plays a significant role in improving the separation of the photogenerated electron-hole pairs to enhance the photocatalytic activity. The band gap energy of a semiconductor can be calculated by the following equation: $\alpha h\nu = A(h\nu - E_g)^{n/2}$, in which α , h , ν , E_g , and A are the absorption coefficient, Planck constant, the light frequency, the band gap, and a constant, respectively. The value of n depends on the type of optical transition of the semiconductor ($n=1$ for direct transition and $n=4$ for indirect transition). For mpg-C₃N₄ and CdLa₂S₄, the n value of 1 is used [15,44]. Therefore, as can be

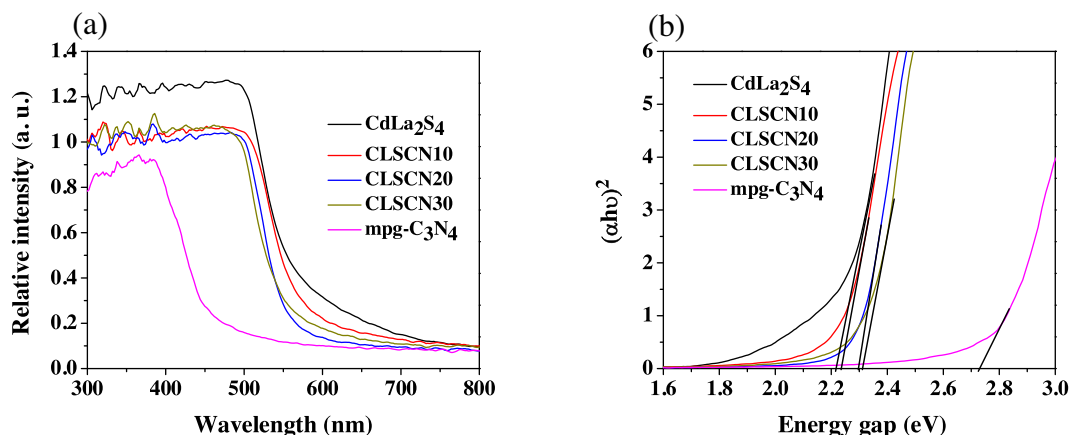


Fig. 5. (a) UV-vis diffuse reflectance spectra of CdLa₂S₄/mpg-C₃N₄ composites and (b) estimated band gap of photocatalyst by Kubelka-Munk function for the as-prepared samples.

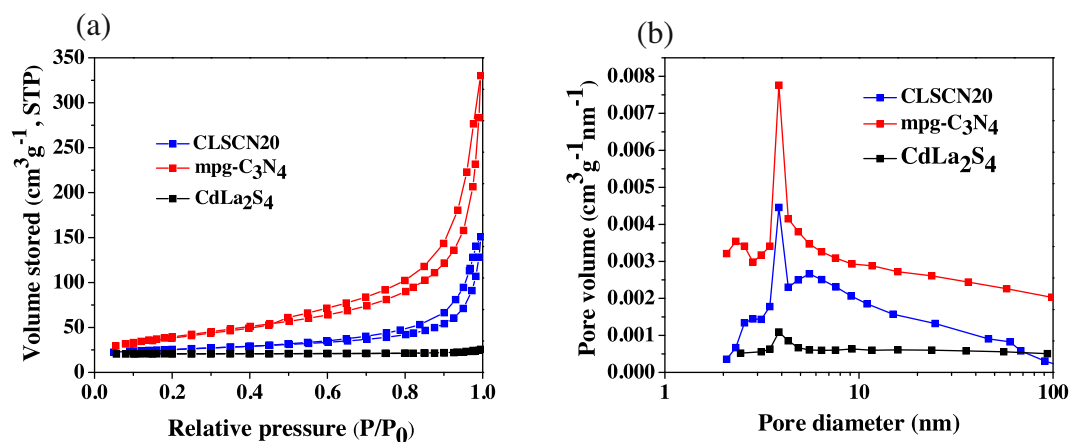


Fig. 6. (a) N₂ adsorption-desorption isotherms and (b) pore size distribution curves of pure CdLa₂S₄, mpg-C₃N₄ and CLSCN20.

seen from Fig. 5b, the corresponding band gap values of CdLa₂S₄, CLSCN10, CLSCN20, CLSCN30 and mpg-C₃N₄ are found to be 2.22, 2.24, 2.30, 2.32 and 2.72 eV, respectively. The valence band edge potentials of the CdLa₂S₄/mpg-C₃N₄ composites were calculated by the following equation:

$$E_{VB} = X - E^e + 0.5E_g,$$

where E_{VB} represents valence band edge potential, X is the electronegativity of the semiconductor estimated by the geometric mean of the electronegativity of the constituent atoms. E^e is the energy of free electrons on the hydrogen scale (~ 4.5 eV), E_g is the band gap energy of the semiconductor. The CB edge potential (E_{CB}) can be determined by $E_{CB} = E_{VB} - E_g$. The X value of pure CdLa₂S₄ and mpg-C₃N₄ is about 5.19 and 4.63 eV [15,45]. The E_{VB} of bare CdLa₂S₄ and mpg-C₃N₄ can be assigned to be +1.80 and +1.49 eV, respectively, and the corresponding E_{CB} of CdLa₂S₄ and mpg-C₃N₄ can be estimated to be -0.42 and -1.23 eV, respectively.

The texture structures of pure CdLa₂S₄, mpg-C₃N₄ and CLSCN20 were characterized via N₂ adsorption-desorption. As shown in Fig. 6a, pure CdLa₂S₄ shows no hysteresis loop, indicative of no pores existing in the sample [46]. The pristine mpg-C₃N₄ and CLSCN20 exhibit type IV isotherms with a H3 hysteresis loop, confirming the presence of mesoporous structure [46,47]. The pore-size distributions of the samples are estimated using the Barrett-Joyner-Halenda (BJH) method from the desorption branches, as shown in Fig. 6b. It can be seen that pristine mpg-C₃N₄ has a narrow pore size distribution and the main pore

Table 1

H₂ evolution rate and apparent quantum efficiency (EQ) of the as-prepared samples.

Sample	H ₂ evolution rate ($\mu\text{mol h}^{-1} \text{g}^{-1}$)	QE (%)
CdLa ₂ S ₄	779.2	1.1
CLSCN10	3841.9	3.6
CLSCN20	5984.8	7.1
CLSCN30	2348.6	3.1
mpg-C ₃ N ₄	trace	–

size of this sample is about 3.87 nm, which is consistent with the TEM observation. The CLSCN20 sample has some broad pore size distribution compared to the pristine mpg-C₃N₄. Brunauer-Emmett-Teller (BET) analysis reveals that the pristine mpg-C₃N₄ possesses a high specific surface area of 317 m² g⁻¹. The BET specific area of CLSCN20 is measured as 86 m² g⁻¹ greatly larger than pure CdLa₂S₄ (20 m² g⁻¹), which can be attributed to the introduction of mpg-C₃N₄.

3.2. Photocatalytic H₂-production activity

The photocatalytic H₂-production over the as-prepared CdLa₂S₄/mpg-C₃N₄ composites was evaluated under visible light irradiation ($\lambda > 420$ nm) using Na₂S and Na₂SO₃ as sacrificial agents to consume photoinduced holes. As shown in Fig. 7 and Table 1, the photocatalytic H₂-production rate is negligible when mpg-C₃N₄ alone is used as photocatalyst due to fast recombination of photocatalytic electron-hole pairs, indicating that pure mpg-C₃N₄

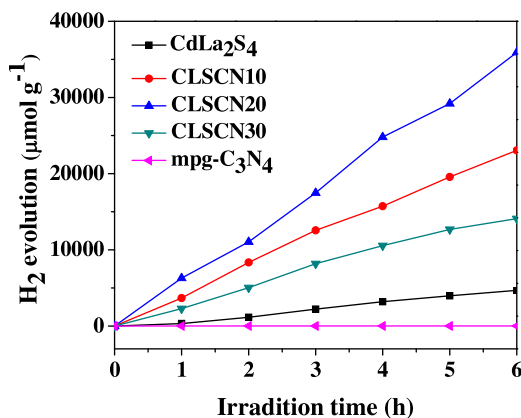


Fig. 7. Plots of photocatalytic H₂ evolution amount vs. irradiation time for as-synthesized samples.

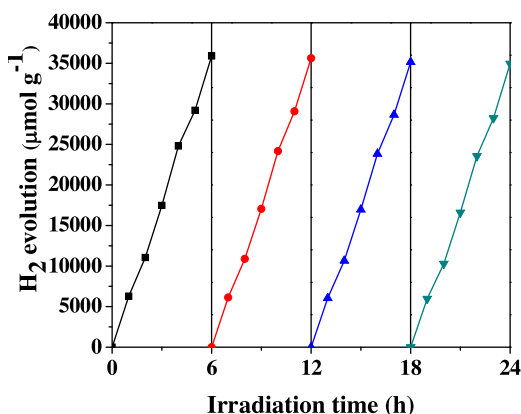


Fig. 8. Cycle runs of the photocatalytic H₂ production over the CLSCN20 sample.

is not active for photocatalytic hydrogen production. Pure CdLa₂S₄ without mpg-C₃N₄ shows some photocatalytic H₂-production activity, but the rate of H₂ evolution is low (779.2 μmol h⁻¹ g⁻¹). After introduction of mpg-C₃N₄, the H₂-production performance of CdLa₂S₄ is significant enhanced. The photoactivity of the CdLa₂S₄/mpg-C₃N₄ composites is found to be dependent on the content of mpg-C₃N₄. With increasing the content of mpg-C₃N₄ from 10 wt% to 20 wt%, the photocatalytic H₂ evolution rate of the hybrid catalyst increases from 3841.9 to 5984.8 μmol h⁻¹ g⁻¹ and the apparent quantum efficiency (QE) increases from 3.6% to 7.1%. A further increase in the content of mpg-C₃N₄ leads to a reduction in the photocatalytic activity. The maximum photocatalytic H₂ generation rate (5984.8 μmol h⁻¹ g⁻¹) is obtained when the mpg-C₃N₄ content is 20 wt%, which is about 7.7 times higher than that of pure CdLa₂S₄. Notably, the photocatalytic H₂-production activity of the CdLa₂S₄/mpg-C₃N₄ (20%) sample is also higher than the various g-C₃N₄-based and CdLa₂S₄-based photocatalysts reported previously [11,14–16,48–57].

The stability and reusability of the CdLa₂S₄/mpg-C₃N₄ hybrid photocatalysts were evaluated by the cycling hydrogen evolution experiment and the results are shown in Fig. 8. The results demonstrate that no obvious decrease of H₂ evolution rate is observed after four consecutive cycles, indicating the good stability of the CdLa₂S₄/mpg-C₃N₄ composite during photocatalytic reactions.

3.3. Possible mechanism of enhanced photocatalytic activity of CdLa₂S₄/mpg-C₃N₄ composite

It has been widely accepted that the separation efficiency of electrons and holes played a crucial role in the

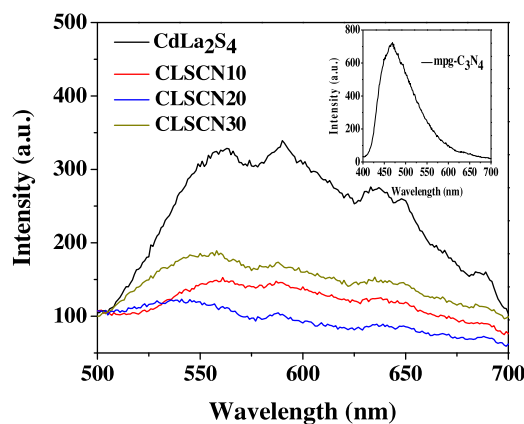


Fig. 9. PL spectra of CdLa₂S₄, mpg-C₃N₄ and CdLa₂S₄/mpg-C₃N₄ composites.

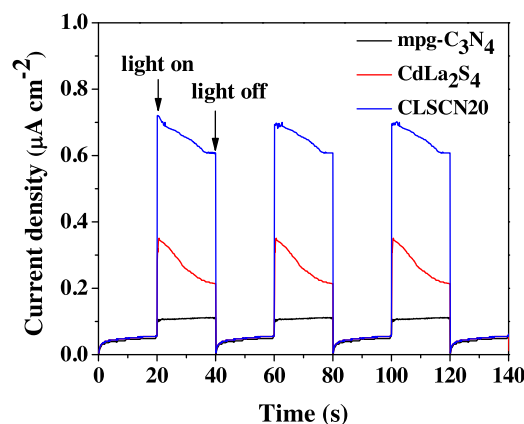


Fig. 10. Transient photocurrent response of pure mpg-C₃N₄, CdLa₂S₄ and CLSCN20 under visible light irradiation.

photocatalytic reaction. Photoluminescence (PL) analysis is commonly applied to investigate the photoinduced carrier separation efficiency of a semiconductor photocatalyst. Fig. 9 shows the PL spectra of pure mpg-C₃N₄, CdLa₂S₄ and CdLa₂S₄/mpg-C₃N₄ composites monitored at an excitation wavelength of 390 nm. It can be seen that the pure mpg-C₃N₄ shows a strong emission peak at around 460 nm, which corresponds to the band gap recombination of electron-hole pairs of mpg-C₃N₄. Three emitting peaks at around 563, 590 and 633 nm are observed for bare CdLa₂S₄ sample. In comparison with bare CdLa₂S₄ and mpg-C₃N₄, the PL intensities of the CdLa₂S₄/mpg-C₃N₄ composites are much lower, which reveals that the composites have a lower recombination rate of electron-hole pairs. Moreover, the order of PL intensity is mpg-C₃N₄ > CdLa₂S₄ > CLSCN30 > CLSCN10 > CLSCN20, which agrees well with the observed results of their photocatalytic activity mentioned above. The interface charge separation efficiency can be further investigated by the photoelectrochemical technique. Fig. 10 shows the transient photocurrent response of pure mpg-C₃N₄, CdLa₂S₄ and CLSCN20 under visible light irradiation for several on-off cycles. It can be seen that pure mpg-C₃N₄ exhibits very low photocurrent density, which can be attributed to the fast recombination of photogenerated electrons and holes. The CLSCN20 sample shows the highest photocurrent intensity among the three samples. This observation indicates that the formed CdLa₂S₄/mpg-C₃N₄ heterojunctions allow for the more efficient separation of photogenerated electron-hole pairs as compared to the individual mpg-C₃N₄ and CdLa₂S₄. Therefore, it can be concluded that the efficient transfer of photo-induced electrons between CdLa₂S₄ and

mpg-C₃N₄ facilitates the electron-hole separation, which is responsible for the enhanced photocatalytic activity.

The high separation efficiency of photo-generated carriers should be ascribed to the suitable band potentials of mpg-C₃N₄ and CdLa₂S₄. The possible mechanism of separation and transportation of electron-hole pairs at the interface of CdLa₂S₄/mpg-C₃N₄ composite under visible light is proposed and illustrated in Scheme 1. Under the visible light illumination, both mpg-C₃N₄ and CdLa₂S₄ can be excited and engender photogenerated electron-hole pairs. Since the CB edge potential of mpg-C₃N₄ (−1.23 eV) is more negative than that of CdLa₂S₄ (−0.42 eV), and the VB of CdLa₂S₄ (+1.80 eV) is more positive than that of mpg-C₃N₄ (+1.49 eV), the excited-electrons in the CB of mpg-C₃N₄ injected directly into that of CdLa₂S₄, and the excited-holes transferred from the VB of CdLa₂S₄ to that of mpg-C₃N₄. Then the electrons at the CB of CdLa₂S₄ evolved H₂ with reducing the adsorbed H⁺. The holes at the VB of mpg-C₃N₄ were consumed by the sacrificial reagents (Na₂S and Na₂SO₃). In such a way, the photo-generated electron-hole pairs were efficiently separated between mpg-C₃N₄ and CdLa₂S₄. Therefore, the CdLa₂S₄/mpg-C₃N₄ composites exhibited better photocatalytic properties than single mpg-C₃N₄ and CdLa₂S₄ in H₂-production under visible light irradiation.

In addition, heterogeneous photocatalysis is a surface-based process, and a large surface area provides more surface active sites for the adsorption of reactant molecules, making the photocatalytic process more efficient. Thus, the enhanced surface area for the CdLa₂S₄/mpg-C₃N₄ composites should also be responsible for the enhancement of photocatalytic activity.

4. Conclusions

In summary, high-visible-light-active and novel CdLa₂S₄/mpg-C₃N₄ photocatalysts were synthesized for the first time by a facile hydrothermal method. The obtained CdLa₂S₄/mpg-C₃N₄ composites exhibited significantly enhanced visible-light photocatalytic H₂ evolution performance compared with pristine CdLa₂S₄ and mpg-C₃N₄. The optimum loading content of mpg-C₃N₄ is 20 wt% and the corresponding H₂ evolution rate is 5984.8 μmol h^{−1} g^{−1} under visible-light irradiation, which was about 7.7 times higher than pure CdLa₂S₄. The remarkable enhancement of photocatalytic activity can be attributed to the improved photo-induced electron-hole pair separation and enhanced specific surface areas. Moreover, the CdLa₂S₄/mpg-C₃N₄ photocatalysts exhibited good recyclability under visible-light irradiation. The excellent properties make the CdLa₂S₄/mpg-C₃N₄ composites as potential candidates in hydrogen evolution application.

Acknowledgments

The authors gratefully acknowledge the National Natural Science Foundation of China (11472164) and Innovative Research Team (IRT13078) for financial support. The authors also thank Lab for Microstructure, Instrumental Analysis and Research Center, Shanghai University, for materials characterizations.

References

- [1] A. Fujishima, K. Honda, *Nature* 238 (1972) 37–38.
- [2] H. Tong, S.X. Ouyang, Y.P. Bi, N. Umezawa, M. Oshikiri, J.H. Ye, *Adv. Mater.* 24 (2012) 229–251.
- [3] C. Kong, S.X. Min, G.X. Lu, *Chem. Commun.* 50 (2014) 5037–5039.
- [4] G.C. Xie, K. Zhang, B.D. Guo, Q. Liu, L. Fang, J.R. Gong, *Adv. Mater.* 25 (2013) 3820–3839.
- [5] K. Zhang, L.J. Guo, *Catal. Sci. Tech.* 3 (2013) 1672–1690.
- [6] H.Y. Li, H.W. Yu, L. Sun, J.L. Zhai, X.R. Han, *Nanoscale* 7 (2015) 1610–1615.
- [7] Y. Noda, B. Lee, K. Domen, J.N. Kondo, *Chem. Mater.* 20 (2008) 5361–5367.
- [8] J.G. Hou, C. Yang, H.J. Cheng, Z. Wang, S.Q. Jiao, H.M. Zhu, *Phys. Chem. Chem. Phys.* 15 (2013) 15660–15668.
- [9] K. Maeda, K. Domen, *Chem. Mater.* 22 (2010) 612–623.
- [10] X.C. Wang, K. Maeda, A. Thomas, K. Takanabe, G. Xin, J.M. Carlsson, K. Domen, M. Antonietti, *Nat. Mater.* 8 (2009) 76–80.
- [11] B.B. Kale, J.O. Baeg, K.J. Kong, S.J. Moon, L.K. Nikam, K.R. Patil, *J. Mater. Chem.* 21 (2011) 2624–2631.
- [12] H. Liu, Z.T. Jin, Z.Z. Xu, *Dalton Trans.* 44 (2015) 14368–14375.
- [13] G.J. Xing, H.L. Guo, P. Li, G.M. Wu, *Appl. Mech. Mater.* 556–562 (2014) 362–365.
- [14] H. Miao, H.Q. Li, Y.M. Cui, D.L. Tao, G. Wang, Y.X. Zhou, *Mater. Lett.* 133 (2014) 281–284.
- [15] J.G. Hou, C. Yang, Z. Wang, S.Q. Jiao, H.M. Zhu, *RSC Adv.* 2 (2012) 10330–10336.
- [16] Y.P. Yuan, S.W. Cao, L.S. Yin, L. Xu, C. Xue, *Int. J. Hydrogen Energy* 38 (2013) 7218–7223.
- [17] S.W. Cao, T.G. Yu, *J. Phys. Chem. Lett.* 5 (2014) 2101–2107.
- [18] J. Mao, T.Y. Peng, X.H. Zhang, K. Li, L.Q. Ye, L. Zan, *Catal. Sci. Technol.* 3 (2013) 1253–1260.
- [19] H.X. Zhao, H.T. Yu, X. Quan, S. Chen, H.M. Zhao, H. Wang, *RSC Adv.* 4 (2014) 624–628.
- [20] F.Z. Su, S.C. Mathew, G. Lipner, X.Z. Fu, M. Antonietti, S. Blechert, X.C. Wang, *J. Am. Chem. Soc.* 132 (2010) 16299–16301.
- [21] J.S. Zhang, F.S. Guo, X.C. Wang, *Adv. Funct. Mater.* 23 (2013) 3008–3014.
- [22] Y. Wang, X.C. Wang, M. Antonietti, Y.J. Zhang, *ChemSusChem* 3 (2010) 435–439.
- [23] X.C. Wang, K. Maeda, X.F. Chen, K. Takanabe, K. Domen, Y.D. Hou, X.Z. Fu, M. Antonietti, *J. Am. Chem. Soc.* 131 (2009) 1680–1681.
- [24] J. Xu, Y.J. Wang, Y.F. Zhu, *Langmuir* 29 (2013) 10566–10572.
- [25] X.F. Chen, J.S. Zhang, X.Z. Fu, M. Antonietti, X.C. Wang, *J. Am. Chem. Soc.* 131 (2009) 11658–11659.
- [26] X.C. Wang, X.F. Chen, A. Thomas, X.Z. Fu, M. Antonietti, *Adv. Mater.* 21 (2009) 1609–1612.
- [27] Y. Wang, J.S. Zhang, X.C. Wang, M. Antonietti, H.R. Li, *Angew. Chem. Int. Ed.* 49 (2010) 3356–3359.
- [28] G. Liu, P. Niu, C.H. Sun, S.C. Smith, Z.G. Chen, G.Q. Lu, H.M. Cheng, *J. Am. Chem. Soc.* 132 (2010) 11642–11648.
- [29] N.Y. Cheng, J.Q. Tian, Q. Liu, C.J. Ge, A.H. Qusti, A.M. Asiri, A.O. Al-Youbi, X.P. Sun, *ACS Appl. Mater. Interfaces* 5 (2013) 6815–6819.
- [30] Y.Y. Bu, Z.Y. Chen, W.B. Li, *Appl. Catal. B: Environ.* 144 (2014) 622–630.
- [31] Q.J. Xiang, J.G. Yu, M. Jaroniec, *J. Phys. Chem. C* 115 (2011) 7355–7363.
- [32] S. Kumar, A. Baruah, S. Tonda, B. Kumar, V. Shanker, B. Sreedhar, *Nanoscale* 6 (2014) 4830–4842.
- [33] F. Yang, V. Kuznetsov, M. Lublow, C. Merschjann, A. Steigert, J. Klaer, A. Thomas, T.S. Niedrig, *J. Mater. Chem. A* 1 (2013) 6407–6415.
- [34] Y. Hou, Z.H. Wen, S.M. Cui, X.R. Guo, J.H. Chen, *Adv. Mater.* 25 (2013) 6291–6297.
- [35] S.C. Yan, S.B. Lv, Z.S. Li, Z.G. Zou, *Dalton Trans.* 39 (2010) 1488–1491.
- [36] Y.L. Chen, J.H. Li, Z.H. Hong, B. Shen, B.Z. Lin, B.F. Gao, *Phys. Chem. Chem. Phys.* 16 (2014) 8106–8113.
- [37] S.C. Yan, Z.S. Li, Z.G. Zou, *Langmuir* 25 (2009) 10397–10401.
- [38] H.F. Li, H.T. Yu, S. Chen, H.M. Zhao, Y.B. Zhang, X. Quan, *Dalton Trans.* 43 (2014) 2888–2894.
- [39] L.Q. Ye, J.Y. Liu, Z. Jiang, T.Y. Peng, L. Zan, *Appl. Catal. B: Environ.* 142–143 (2013) 1–7.
- [40] L. Ge, F. Zuo, J.K. Liu, Q. Ma, C. Wang, D.Z. Sun, L. Bartels, P.Y. Feng, *J. Phys. Chem. C* 116 (2012) 13708–13714.
- [41] H.D. Zhang, M. Yu, J.C. Zhang, C.H. Sheng, X. Yan, W.P. Han, Y.C. Liu, S. Chen, G.Z. Shen, Y.Z. Long, *Nanoscale* 7 (2015) 10513–10518.
- [42] S.Q. Tian, Y.P. Zhang, D.W. Zeng, H. Wang, N. Li, C.S. Xie, C.X. Pan, X.J. Zhao, *Phys. Chem. Chem. Phys.* 17 (2015) 27437–27445.
- [43] K. Kim, J. Jeong, A.K. Azad, S.B. Jin, J.H. Kim, *Appl. Surf. Sci.* 365 (2016) 38–46.
- [44] Y.Q. Shi, S.H. Jiang, K.Q. Zhou, B.B. Wang, B. Wang, Z. Gui, Y. Hu, R.K.K. Yuen, *RSC Adv.* 4 (2014) 2609–2613.
- [45] S.M. Wang, D.L. Li, C. Sun, S.G. Yang, Y. Guan, H. He, *Appl. Catal. B: Environ.* 144 (2014) 885–892.
- [46] L. Shi, L. Liang, J. Ma, F.X. Wang, J.M. Sun, *Dalton Trans.* 43 (2014) 7236–7244.
- [47] D.L. Jiang, L.L. Chen, J.J. Zhu, M. Chen, W.D. Shi, J.M. Xie, *Dalton Trans.* 42 (2013) 15726–15734.
- [48] J.G. Yu, S.H. Wang, B. Cheng, Z. Lin, F. Huang, *Catal. Sci. Technol.* 3 (2013) 1782–1789.
- [49] Z.H. Chen, P. Sun, B. Fan, Z.G. Zhang, X.M. Fang, *J. Phys. Chem. C* 118 (2014) 7801–7807.
- [50] L.S. Yin, Y.P. Yuan, S.W. Cao, Z.Y. Zhang, C. Xue, *RSC Adv.* 4 (2014) 6127–6132.
- [51] L. Ge, C.C. Han, X.L. Xiao, L.L. Guo, *Int. J. Hydrogen Energy* 38 (2013) 6960–6969.
- [52] D.L. Jiang, L.L. Chen, J.M. Xie, M. Chen, *Dalton Trans.* 43 (2014) 4878–4885.
- [53] J.X. Wang, J. Huang, H.L. Xie, A.L. Qu, *Int. J. Hydrogen Energy* 39 (2014) 6354–6363.
- [54] J. Chen, S.H. Shen, P.H. Guo, M. Wang, P. Wu, X.X. Wang, L.J. Guo, *Appl. Catal. B: Environ.* 152–153 (2014) 335–341.
- [55] H. Katsumata, Y. Tachi, T. Suzuki, S. Kaneco, *RSC Adv.* 4 (2014) 21405–21409.
- [56] S.W. Cao, X.F. Liu, Y.P. Yuan, Z.Y. Zhang, Y.S. Liao, J. Fang, S.C.J. Loo, T.C. Sum, C. Xue, *Appl. Catal. B: Environ.* 147 (2014) 940–946.
- [57] L. Ge, C.C. Han, X.L. Xiao, L.L. Guo, *Appl. Catal. B: Environ.* 142–143 (2013) 414–422.